

Article

Hazardous Doping for Photo-Electrochemical Conversion: The Case of Nb-Doped Fe₂O₃ from First Principles

Natav Yatom and Maytal Caspary Toroker *

Received: 2 October 2015 ; Accepted: 26 October 2015 ; Published: 4 November 2015

Academic Editor: Sergei Manzhos

Department of Materials Science and Engineering, Technion—Israel Institute of Technology, Haifa 32000, Israel; nyatom@tx.technion.ac.il

* Correspondence: maytal@tx.technion.ac.il; Tel.: +972-4-829-4298

Abstract: The challenge of improving the efficiency of photo-electrochemical devices is often addressed through doping. However, this strategy could harm performance. Specifically, as demonstrated in a recent experiment, doping one of the most widely used materials for water splitting, iron(III) oxide (Fe₂O₃), with niobium (Nb) can still result in limited efficiency. In order to better understand the hazardous effect of doping, we use Density Functional Theory (DFT)+U for the case of Nb-doped Fe₂O₃. We find a direct correlation between the charge of the dopant, the charge on the surface of the Fe₂O₃ material, and the overpotential required for water oxidation reaction. We believe that this work contributes to advancing our understanding of how to select effective dopants for materials.

Keywords: water splitting; Density Functional Theory; DFT+U; iron oxides; doping

1. Introduction

Improving the efficiency of solar energy conversion in a photo-electrochemical device is challenging. Achieving the goal of enhancing efficiency relies on at least two material properties: one is having high charge conductivity and the second is having good catalytic ability [1]. Unfortunately, one of the commonly used materials for water splitting, iron(III) oxide (Fe₂O₃), lacks both these properties [2].

Successful advances have been demonstrated with point defects such as doping [3–8]. N-type doping of Fe₂O₃ with elements such as Ti or Si increases the number of electron charge carriers and therefore can boost electron conductivity [9,10]. Furthermore, Si has an advantage over Ti since the latter creates low energy states that can “trap” electron carriers [11]. Therefore, selecting dopants carefully is crucial for improving electron conductivity.

Despite improvements in electronic conductivity, recent studies show that doping can harm catalysis. For example, doping Fe₂O₃ with Ti, Si, or Pt can unfavorably increase the overpotential for water oxidation [12–14]. The trends in changing the overpotential upon doping was related to the adsorbing energies of the reaction intermediates. Among several dopants that were considered, the most effective dopants for favorably reducing the overpotential were discovered to be Ni and Co [12].

In this paper, we use Density Functional Theory (DFT)+U in order to demonstrate how n-type doping could be hazardous for catalysis. This is the first study where we calculate the free energies involved in water oxidation of Nb-doped Fe₂O₃. We select the Nb dopant for two reasons. First, recent experiments show that doping Fe₂O₃ with Nb unfavorably increases overpotential [15]. Second, Nb has a formal charge of +5 which is lower than the charge of +4 in conventional n-type

dopants of Fe₂O₃. We find that Nb overcharges the surface of Fe₂O₃ and that this has a direct consequence on catalysis.

2. Computational Details

The VASP simulation package (5.3 version, VASP group at University of Vienna, Vienna, Austria) was used for all spin-polarized Density Functional Theory (DFT) calculations [16,17] with the PBE (Perdew, Burke, and Ernzerhof) [18] exchange-correlation (XC) functional. We chose the Dudarev *et al.* DFT+U formalism [19] because it better describes the strong correlated electrons of first row transition metals [20–23]. An *ab-initio* derived value of $U - J = 4.3$ eV [24] was chosen for Fe atoms, while zero for O, Nb and H atoms that are closed-shell in their corresponding stable oxidation states. Nuclei and core electrons were described by PAW potentials [25,26] such that only the 6, 14, 11 and 1 valence electrons of O-2s²2p⁴, Fe-3p⁶3d⁶4s², Nb-4p⁶5s¹4d⁴, and H-1s¹, respectively, were considered explicitly.

Several computational settings were used to achieve convergence. Ion positions were relaxed using conjugated gradient method and the stopping criterion for the ionic relaxation was chosen for all forces to be smaller than 3×10^{-2} eV/Å. No symmetry was imposed. An energy cutoff of 700 eV converged the total energy to less than 1 meV per atom. $4 \times 4 \times 4$ and $3 \times 3 \times 1$ gamma-centered k-space grid for the bulk and surface, respectively converged the total energy to 1 meV. Ionic relaxation was done with Gaussian smearing method with smearing width of 0.01 eV for fast relaxation, and the last iteration was done with Tetrahedron method with Blöchl corrections [27,28].

The primitive unit cell of Fe₂O₃ is rhombohedral and contains two Fe₂O₃ stoichiometric units. Bulk unit cells were cleaved at the (0001) plane which is one of stable surfaces of Fe₂O₃ [29,30]. Due to similarity of ionic radii [31], the Nb was inserted in the slab as an Fe substitution defect and not as interstitial defect as detected experimentally [32]. Although Nb has some solubility in Fe₂O₃ of up to 2 ± 1 at% [33], we chose to substitute Nb in a slab with 32 atoms (7 at%) in order to have a direct comparison to pervious calculations with other dopants using the same level of theory (DFT+U) [12]. Furthermore, when we use a longer slab with 39 atoms (5 at%) the overpotential changes by less than 0.02 eV. In addition, previous calculations show little dependence of doping concentration on the calculated free energies [12]. The initial position of terminating hydrogen atoms was placed according to the information given in previous calculations [12]. We do not include additional water molecules above the slab since previous work showed that the first water monolayer has little influence on the calculated free energies [12]. All slab calculations were converged with a 10 [Å] vacuum.

The analysis is based on the conventional approach developed by Nørskov for modeling surface chemistry. The model is based on having a series of surface slab models representing intermediate reactions. The free energy required for each reaction step is calculated by solving the Kohn-Sham equations self-consistently for each reaction intermediate. We consider the following mechanism for water oxidation, as previously suggested [34]:

- (1) $H_2O + * \rightarrow *OH_2$
- (2) $*OH_2 \rightarrow *OH + H^+ + e^-$
- (3) $*OH \rightarrow *O + H^+ + e^-$
- (4) $H_2O + *O \rightarrow *OOH + H^+ + e^-$
- (5) $*OOH \rightarrow O_2 + * + H^+ + e^-$

where * denotes oxygen vacancy site on the surface and *OH₂, *OH, *O, and *OOH are adsorbates. The corresponding free energies were calculated by subtracting the total energies of reactants and products (for example, ΔG_1 is calculated for reaction 1. We added the reported zero point energy (ZPE) corrections and entropic contributions of pure Fe₂O₃ since composition was shown to have a

negligible effect on the results [12]. The overpotential (O.P) is defined as voltage needed to add to the calculated electrochemical potential of:

$$\frac{\sum_{i=1}^5 \Delta G_i}{4e} = \frac{\Delta G_{(2H_2O(l) \rightarrow 2H_2(g) + O_2(g))}}{4e} = \frac{4.43 [eV]}{4e} = 1.11 [V] \quad (1)$$

in order to obtain the reaction potential:

$$\Phi_{rx} = \frac{\max\{\Delta G_i\}_{i=1}^5}{e} \quad (2)$$

in which all reaction steps free energies are negative, such that the reaction is thermodynamic spontaneous:

$$\text{O.P} = \Phi_{rx} - 1.11 [V] \quad (3)$$

3. Results and Discussion

This section contains our free energy calculations for water oxidation on Nb-doped $\text{Fe}_2\text{O}_3(0001)$ and a comparison to previously-studied undoped Fe_2O_3 and Ni- and Pt-doped Fe_2O_3 . We find that the overpotential upon Nb doping is largest, according to the following relation: $\text{Nb} > \text{Pt} > \text{Fe} > \text{Ni}$, which we correlate to the oxidation states $\text{Nb}^{+5} > \text{Pt}^{+4} > \text{Fe}^{+3} > \text{Ni}^{+2}$, as detailed below.

Calculating the free energies for Nb-doped Fe_2O_3 surface reveals that the first chemical bond breaking is favorable (as seen in Figure 1, $\Delta G_2 = -1.14$ eV). This first dehydrogenation is thermodynamically easy since reaction 2 involves extracting an electron from a surface that contains excess Nb-donated electrons. The negative free energy at the first dehydrogenation is compensated by a large free energy at later reaction steps. Subsequent reaction intermediates have less electron charge and therefore are more stable and have a corresponding larger free energy. As a result, the overpotential significantly increases upon Nb doping.

That is, the amount of charge generated by the dopant at the surface affects the overpotential. Since Nb generates two electrons, the free energies involved in taking away these excess electrons are negative (as seen in Figure 1, reactions 2 and 3). The number of electrons generated depends on the atom type and since the surface prefers to remain neutrally charged then this also affects the overpotential.

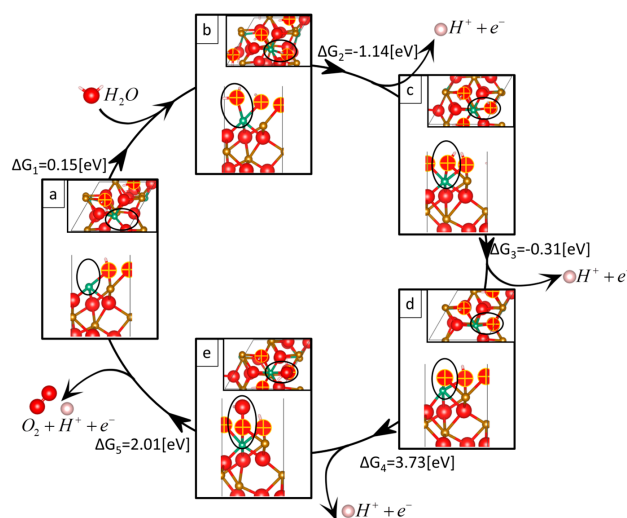


Figure 1. Catalytic cycle of the water oxidation reaction on Nb-doped $\text{Fe}_2\text{O}_3(0001)$. Red, gold, green, and white spheres represent O, Fe, Nb, and H atoms, respectively. The insets show a top view of each reaction intermediate slab structure. The active site is circled in black. Created with VESTA [35].

The overpotential for water oxidation on Fe_2O_3 depends on the dopant atom type. As seen in Table 1 and Figure 2, the overpotential can be ranked according to the following relation: $\text{Nb} > \text{Pt} > \text{Fe} > \text{Ni}$, where Nb doping generates the highest overpotential.

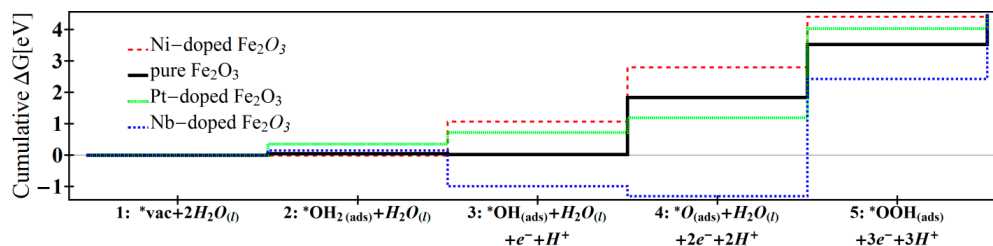


Figure 2. Cumulative free energies for water oxidation on Ni-doped, pure, Pt-doped, Nb-doped Fe_2O_3 . Values for non-Nb doped materials are obtained from refs [12,13].

The high overpotential required to induce water oxidation in Nb-doped Fe_2O_3 results from the surface charging brought by the dopant. For example, in contrast to Nb doping, Ni does not donate excess electrons and the first dehydrogenation in Ni-doped Fe_2O_3 requires a positive free energy ($\Delta G_2 = 1.08$ eV). Free energy is required to extract a proton and an electron from the water-adsorbed surface that prefers to stay neutrally charged. The rest of the free energy needed to oxidize water is distributed over three dehydrogenation reactions (as seen in Table 1: reactions 2–4). As a whole, doping Fe_2O_3 with Ni results in the best and lowest overpotential.

Table 1. Free energies of intermediate water oxidation reactions for Ni-doped, pure, Pt-doped, and Nb-doped Fe_2O_3 . Units are in eV.

	Reaction 1	Reaction 2	Reaction 3	Reaction 4	Reaction 5	Overpotential
Ni-doped [12]	−0.01	1.08	1.73	1.61	0.03	0.62
Pure [12]	0.05	−0.03	1.82	1.68	0.91	0.71
Pt-doped [13]	0.35	0.36	0.47	2.83	0.40	1.72
Nb-doped	0.15	−1.14	−0.31	3.73	2.01	2.62

Therefore, the charge of the dopant has a critical role. The Nb dopant is n-type in Fe_2O_3 and has a corresponding oxidation state of +5 (according to a Müllikan magnetic moment of zero). This can be visualized in Figure 3, where Nb donates two electrons that are located on two iron atoms.

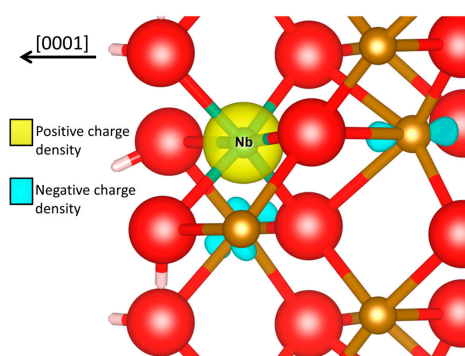


Figure 3. Charge density difference plot for the $^*\text{OH}$ intermediate of Nb-doped *vs.* pure Fe_2O_3 . Calculated by subtracting the electron density of the pure Fe_2O_3 from the Nb-doped Fe_2O_3 $^*\text{OH}$ intermediate at the fixed ionic positions of the latter. Red, gold, green and white spheres denote O, Fe, Nb and H atoms, respectively. Negative and positive charge density iso-surfaces (± 0.07 [e/Bohr³]) are in blue and yellow, respectively, where negative being absence of electrons. Created with VESTA visualizing software [35].

Therefore, Nb donates twice as much charge compared to the Pt dopant which we have recently studied and has an oxidation state of +4 [13]. In contrast, previous calculations show that Ni is a p-type dopant and has an oxidation state of +2 [12]. Therefore, the relation between the oxidation states is: $\text{Nb}^{+5} > \text{Pt}^{+4} > \text{Fe}^{+3} > \text{Ni}^{+2}$, where Nb charges the Fe_2O_3 surface the most.

Finally, the results can be positioned on a Volcano curve that correlates between the reaction potential Φ_{rx} and the surface binding energy of adsorbates [12,34,36–38]. As can be seen in Figure 4, the reaction potential Φ_{rx} for Nb is located on the Volcano curve that was previously obtained for other dopants of Fe_2O_3 (dashed line in Figure 4) [12], and therefore maintains the known scaling relationship between overpotential and reactants adsorption energies. Nb is positioned at the lower part of the curve with an outstandingly high reaction potential Φ_{rx} (Figure 4) and overpotential (Equation (3)).

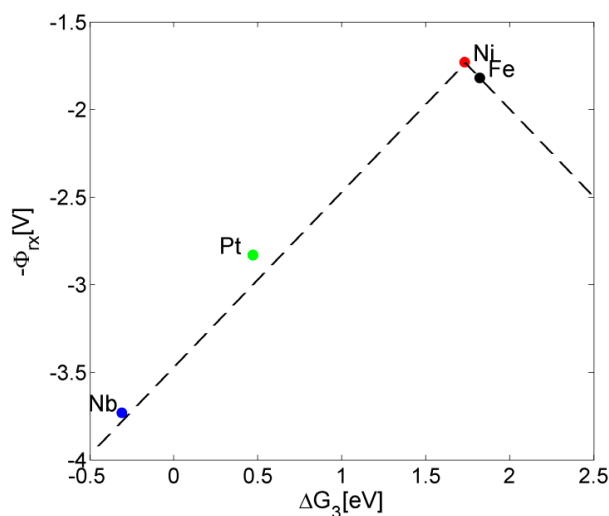


Figure 4. Volcano plot for Fe_2O_3 showing location of Nb-doping at the far end of the curve.

4. Conclusions

We modeled water oxidation on Nb-doped $\text{Fe}_2\text{O}_3(0001)$ and found that the overpotential is significantly higher than for pure Fe_2O_3 or for Fe_2O_3 doped with elements that have a smaller oxidation state than Nb^{+5} . We explained this hazardous effect of increasing the overpotential in terms of surface charging: overcharging the surface at the beginning of the reaction via Nb-doping causes the first as well as the second dehydrogenation to be thermodynamically spontaneous (as we can see in Table 1, reactions 2 and 3 have a negative ΔG for the Nb-doped case). Overall, the free energies are not distributed evenly throughout the reaction intermediates and therefore the overpotential is extremely large. By comparing to other dopants studied previously in the literature, we find a direct correlation between the reaction overpotential and the oxidation state of the dopant. Our results agree with experiment that show an increase in overpotential upon Nb-doping [15]. However, we note that previous experiments show that water splitting efficiency improves upon doping with Nb [15,39,40], probably since other factors, such as band gap, band edge positions, and electronic conductivity affect the overall photon-to-hydrogen conversion efficiency; we shall address other effects of Nb in our next publication. We envision that our new understanding of the effect of doping on water oxidation will be useful for selecting effective dopants for surface catalysis.

Supplementary Material

Unit cell geometries are provided. Supplementary materials can be accessed at: <http://www.mdpi.com/1420-3049/20/11/19668/s1>.

Acknowledgments: This research was supported by the Morantz Energy Research Fund, the Nancy and Stephen Grand Technion Energy Program, the I-CORE Program of the Planning and Budgeting Committee, and The Israel Science Foundation (Grant No. 152/11).

Author Contributions: N.Y. performed the calculations. N.Y. and M.C.T wrote the paper. M.C.T supervised the project.

Conflicts of Interest: The authors declare no conflict of interest.

References

1. Kemppainen, E.; Halme, J.; Lund, P. Physical Modeling of Photoelectrochemical Hydrogen Production Devices. *J. Phys. Chem. C* **2015**, *119*, 21747–21766. [[CrossRef](#)]
2. Zandi, O.; Hamann, T.W. The potential *versus* current state of water splitting with hematite. *PCCP* **2015**, *17*, 22485–22503. [[CrossRef](#)] [[PubMed](#)]
3. Monllor-Satoca, D.; Bartsch, M.; Fabrega, C.; Genc, A.; Hilaire, S.; Andreu, T.; Arbiol, J.; Niederberger, M.; Morante, J.R. What Do you Do, Titanium? Insight into the Role of Titanium Oxide as Water Oxidation Promoter in Hematite-based Photoanodes. *Energy Environ. Sci.* **2015**. [[CrossRef](#)]
4. Wang, D.; Chen, H.; Chang, G.; Lin, X.; Zhang, Y.; Aldalbahi, A.; Peng, C.; Wang, J.; Fan, C. Uniform Doping of Titanium in Hematite Nanorods for Efficient Photoelectrochemical Water Splitting. *ACS Appl. Mater. Interfaces* **2015**, *7*, 14072–14078. [[CrossRef](#)] [[PubMed](#)]
5. Abel, A.J.; Garcia-Torregrosa, I.; Patel, A.M.; Opananont, B.; Baxter, J.B. SILAR-deposited Hematite Films for Photoelectrochemical Water Splitting: Effects of Sn, Ti, Thickness, and Nanostructuring. *J. Phys. Chem. C* **2015**, *119*, 4454–4465. [[CrossRef](#)]
6. Wang, Z.; Liu, G.; Ding, C.; Chen, Z.; Zhang, F.; Shi, J.; Li, C. Synergetic Effect of Conjugated Ni(OH)₂/IrO₂ Cocatalyst on Titanium-Doped Hematite Photoanode for Solar Water Splitting. *J. Phys. Chem. C* **2015**, *119*, 19607–19612.
7. Yang, T.-Y.; Kang, H.-Y.; Sim, U.; Lee, Y.-J.; Lee, J.-H.; Koo, B.; Nam, K.T.; Joo, Y.-C. A new hematite photoanode doping strategy for solar water splitting: Oxygen vacancy generation. *PCCP* **2013**, *15*, 2117–2124. [[CrossRef](#)] [[PubMed](#)]
8. Lee, J.; Han, S. Thermodynamics of native point defects in [small alpha]-Fe₂O₃: An ab initio study. *PCCP* **2013**, *15*, 18906–18914. [[CrossRef](#)] [[PubMed](#)]
9. Kronawitter, C.X.; Zegkinoglou, I.; Shen, S.H.; Liao, P.; Cho, I.S.; Zandi, O.; Liu, Y.S.; Lashgari, K.; Westin, G.; Guo, J.H.; *et al.* Titanium incorporation into hematite photoelectrodes: Theoretical considerations and experimental observations. *Energy Environ. Sci.* **2014**, *7*, 3100–3121. [[CrossRef](#)]
10. Chatman, S.; Pearce, C.I.; Rosso, K.M. Charge Transport at Ti-Doped Hematite (001)/Aqueous Interfaces. *Chem. Mater.* **2015**, *27*, 1665–1673. [[CrossRef](#)]
11. Liao, P.; Toroker, M.C.; Carter, E.A. Electron Transport in Pure and Doped Hematite. *Nano Lett.* **2011**, *11*, 1775–1781. [[CrossRef](#)] [[PubMed](#)]
12. Liao, P.; Keith, J.A.; Carter, E.A. Water oxidation on pure and doped hematite (0001) surfaces: Prediction of Co and Ni as effective dopants for electrocatalysis. *J. Am. Chem. Soc.* **2012**, *134*, 13296–13309. [[CrossRef](#)] [[PubMed](#)]
13. Neufeld, O.; Toroker, M.C. Platinum-Doped α -Fe₂O₃ for Enhanced Water Splitting Efficiency: A DFT+U Study. *J. Phys. Chem. C* **2015**, *119*, 5836–5847. [[CrossRef](#)]
14. Toroker, M.C. Theoretical Insights into the Mechanism of Water Oxidation on Nonstoichiometric and Titanium-Doped Fe₂O₃(0001). *J. Phys. Chem. C* **2014**, *118*, 23162–23167. [[CrossRef](#)]
15. Aroutiounian, V.M.; Arakelyan, V.M.; Shahnazaryan, G.E.; Stepanyan, G.M.; Khachaturyan, E.A.; Wang, H.; Turner, J.A. Photoelectrochemistry of semiconductor electrodes made of solid solutions in the system Fe₂O₃-Nb₂O₅. *Sol. Energy* **2006**, *80*, 1098–1111. [[CrossRef](#)]
16. Kresse, G.; Hafner, J. Ab initio molecular dynamics for liquid metals. *Phys. Rev. B* **1993**, *47*, 558–561. [[CrossRef](#)]
17. Kresse, G.; Furthmüller, J. Efficiency of ab-initio total energy calculations for metals and semiconductors using a plane-wave basis set. *Comput. Mater. Sci.* **1996**, *6*, 15–50.
18. Perdew, J.P.; Burke, K.; Ernzerhof, M. Generalized Gradient Approximation Made Simple [Phys. Rev. Lett. **77**, 3865 (1996)]. *Phys. Rev. Lett.* **1997**, *78*, 1396. [[CrossRef](#)]

19. Dudarev, S.; Botton, G.; Savrasov, S.; Humphreys, C.; Sutton, A. Electron-energy-loss spectra and the structural stability of nickel oxide: An LSDA+U study. *Phys. Rev. B* **1998**, *57*, 1505–1509. [[CrossRef](#)]
20. Zhou, F.; Cococcioni, M.; Marianetti, C.A.; Morgan, D.; Ceder, G. First-principles prediction of redox potentials in transition-metal compounds with LDA+U. *Phys. Rev. B* **2004**, *70*, 235121. [[CrossRef](#)]
21. Wang, L.; Maxisch, T.; Ceder, G. Oxidation energies of transition metal oxides within the GGA+U framework. *Phys. Rev. B* **2006**, *73*, 195107. [[CrossRef](#)]
22. Anisimov, V.I.; Aryasetiawan, F.; Lichtenstein, A. First-principles calculations of the electronic structure and spectra of strongly correlated systems: The LDA+U method. *J. Phys. Condens. Matter* **1997**, *9*, 767–808. [[CrossRef](#)]
23. Rollmann, G.; Rohrbach, A.; Entel, P.; Hafner, J. First-principles calculation of the structure and magnetic phases of hematite. *Phys. Rev. B* **2004**, *69*, 1124–1133. [[CrossRef](#)]
24. Mosey, N.J.; Liao, P.; Carter, E.A. Rotationally invariant ab initio evaluation of Coulomb and exchange parameters for DFT+U calculations. *J. Chem. Phys.* **2008**, *129*, 014103. [[CrossRef](#)] [[PubMed](#)]
25. Kresse, G.; Joubert, D. From ultrasoft pseudopotentials to the projector augmented-wave method. *Phys. Rev. B* **1999**, *59*, 1758–1775.
26. Blöchl, P.E. Projector augmented-wave method. *Phys. Rev. B* **1994**, *50*, 17953–17979. [[CrossRef](#)]
27. Blöchl, P.E.; Jepsen, O.; Andersen, O.K. Improved tetrahedron method for Brillouin-zone integrations. *Phys. Rev. B* **1994**, *49*, 16223–16233. [[CrossRef](#)]
28. Lehmann, G.; Taut, M. On the numerical calculation of the density of states and related properties. *Phys. Status Solidi b* **1972**, *54*, 469–477. [[CrossRef](#)]
29. Lad, R.J.; Henrich, V.E. Structure of α -Fe₂O₃ single crystal surfaces following Ar⁺ ion bombardment and annealing in O₂. *Surf. Sci.* **1988**, *193*, 81–93. [[CrossRef](#)]
30. Nguyen, M.-T.; Seriani, N.; Piccinin, S.; Gebauer, R. Photo-driven oxidation of water on α -Fe₂O₃ surfaces: An ab initio study. *J. Chem. Phys.* **2014**, *140*. [[CrossRef](#)] [[PubMed](#)]
31. Shannon, R. Revised effective ionic radii and systematic studies of interatomic distances in halides and chalcogenides. *Acta Crystallogr. Sec. A* **1976**, *32*, 751–767. [[CrossRef](#)]
32. Sanchez, C.; Hendewerk, M.; Sieber, K.D.; Somorjai, G.A. Synthesis, bulk, and surface characterization of niobium-doped Fe₂O₃ single crystals. *J. Solid State Chem.* **1986**, *61*, 47–55. [[CrossRef](#)]
33. Turnock, A.C. Fe-Nb Oxides: Phase Relations at 1180 °C. *J. Am. Ceram. Soc.* **1966**, *49*, 177–180. [[CrossRef](#)]
34. Rossmesl, J.; Qu, Z.-W.; Zhu, H.; Kroes, G.-J.; Nørskov, J.K. Electrolysis of water on oxide surfaces. *J. Electroanal. Chem.* **2007**, *607*, 83–89. [[CrossRef](#)]
35. Momma, K.; Izumi, F. VESTA: A three-dimensional visualization system for electronic and structural analysis. *J. Appl. Crystallogr.* **2008**, *41*, 653–658. [[CrossRef](#)]
36. Valdes, A.; Qu, Z.-W.; Kroes, G.-J.; Rossmesl, J.; Nørskov, J.K. Oxidation and photo-oxidation of water on TiO₂ surface. *J. Phys. Chem. C* **2008**, *112*, 9872–9879. [[CrossRef](#)]
37. Man, I.C.; Su, H.Y.; Calle-Vallejo, F.; Hansen, H.A.; Martínez, J.I.; Inoglu, N.G.; Kitchin, J.; Jaramillo, T.F.; Nørskov, J.K.; Rossmesl, J. Universality in oxygen evolution electrocatalysis on oxide surfaces. *ChemCatChem* **2011**, *3*, 1159–1165.
38. Nørskov, J.K.; Rossmesl, J.; Logadottir, A.; Lindqvist, L.; Kitchin, J.R.; Bligaard, T.; Jonsson, H. Origin of the overpotential for oxygen reduction at a fuel-cell cathode. *J. Phys. Chem. B* **2004**, *108*, 17886–17892. [[CrossRef](#)]
39. Sanchez, C.; Sieber, K.D.; Somorjai, G.A. The photoelectrochemistry of niobium doped α -Fe₂O₃. *J. Electroanal. Chem. Interfacial Electrochem.* **1988**, *252*, 269–290. [[CrossRef](#)]
40. Aroutiounian, V.M.; Arakelyan, V.M.; Shahnazaryan, G.E.; Stepanyan, G.M.; Khachaturyan, E.A.; Turner, J.A. Investigations of the structure of the iron oxide semiconductor-electrolyte interface. *C. R. Chim.* **2006**, *9*, 325–331. [[CrossRef](#)]

Sample Availability: Not apply.



© 2015 by the authors; licensee MDPI, Basel, Switzerland. This article is an open access article distributed under the terms and conditions of the Creative Commons by Attribution (CC-BY) license (<http://creativecommons.org/licenses/by/4.0/>).